Measurement of the Soret and diffusion coefficients for benchmark binary mixtures by means of digital interferometry

A. Mialdun[a)] and V. Shevtsova[b)]

MRC, Université Libre de Bruxelles, CP165/62, Av. F.D. Roosevelt, 50, B-1050 Bruxelles, Belgium

We report on the development of the optical digital interferometry (ODI) technique for measuring diffusion and Soret coefficients. The unique feature of this method is that it traces the *transient* path of the system in the *entire* two-dimensional cross section of a cell. In this way, it is applicable not only for measurements of Soret coefficients, but also for studying diffusive transport mechanism and convection. Presently, this method is not widely used and, in our view, not because of fundamental limitations but rather due to a lack of properly developed postexperimental procedures of the raw data analysis. Thus, in this paper our attention is focused on the successive analysis of different steps: the fringe analysis, the choice of reference images, the thermal design of the cell, and multiparameter fitting procedure. Using the ODI technique, we have measured the diffusion and the Soret coefficients for three binary mixtures composed of dodecane ($C_{12}H_{26}$), isobutylbenzene, and 1,2,3,4-tetrahydronaphtalene at a mean temperature of 25°C and 50 wt. % in each component. These measurements were compared with their benchmark values and show an agreement within less than 3%. © *2011 American Institute of Physics*. [doi:10.1063/1.3546036]

I. INTRODUCTION

Diffusion is a molecular transport of mass in mixtures, which occurs in the presence of a concentration gradient and tends to reduce concentration variations. Mass transport of species caused by the thermal gradient is known as thermal diffusion or the Soret effect.[1] Here, the term "species" may refer to molecules, polymers, or small particles (colloids). There are many important processes in nature and technology, where these phenomena play a crucial role. The composition of hydrocarbon reservoirs might be affected by diffusion as well as the Soret effect (due to the presence of geo-thermal gradient).[2,3] The effect of thermal diffusion is employed for isotope separation in liquid and gaseous mixtures as well as other separation processes[4] that involve colloids, macromolecules, or nanofluides. Another potential applications include high-pressure combustion,[5] solidification processes, oceanic convection,[6] biological systems,[7] and CO_2 geological storage.

Although several theoretical approaches have been presented in the literature, there is no unambiguous theory for thermal diffusion in liquids. So, advanced experimental techniques and accurate data on transport coefficients are of great importance for further theoretical developments and applications. Especially, there exists a clear interest to measurement of transport coefficients in multicomponent mixtures, which firstly demands well established techniques for binary mixtures. The experimental studies of the thermodiffusion in ternary mixtures are done in an early stage. The first steps on the way from binary to ternary systems have already been done.[8–10] However, the results exhibit only mediocre agreement between different sources, therefore introduction of new measuring technique is important for the results verification.

The rising interest in the reliable measurement causes appearance of new approaches,[11,12] revisiting early established techniques[13] and tendency of cross checking the results obtained by different methods.[14,15] For this reason, the Benchmark of Fontainebleau was performed,[14] where several laboratories carried out a quantitative comparison between different experimental methods actively used in 1999–2003 to determine the diffusion, thermal diffusion, and Soret coefficients of three binary liquid mixtures. The Benchmark is still in progress as recently the results from beam deflection technique have been introduced to the benchmark[13] and some actively used methods have not yet contributed into Benchmark database.

The existing methods can be divided into two groups. The first group employs convection arising from compositional and thermal variations in gravity field. In the Rayleigh–Bénard setup, the data are extracted from critical parameters for the oscillatory onset of convection in binary fluid.[16] Thermogravitational column technique[17,18] relies on coupling between convection and horizontal thermal diffusion in a side-heated vertical slot. However, liquid sampling required in this method may disturb the diffusive process.[16]

For the second group, convectionless state is crucial for the measurements. The sampling problem exists in the standard Soret cell,[16] where liquid is placed between two differentially heated copper plates. Modern techniques based on optical methods of observation do not perturb the diffusive process. In the beam deflection technique, the Soret cell has transparent walls and evolution of composition is observed via deflection of a laser beam passing through the medium.[19,20] In the thermal lens technique,[21,22] the temperature gradient is created by heat generation resulting from the absorption of light into the fluid. The sample behaves like an optical lens due to the change of refractive index resulting from thermal and compositional gradients. Another important method is the thermal diffusion forced Rayleigh

---

[a)]Electronic mail: amialdun@ulb.ac.be.
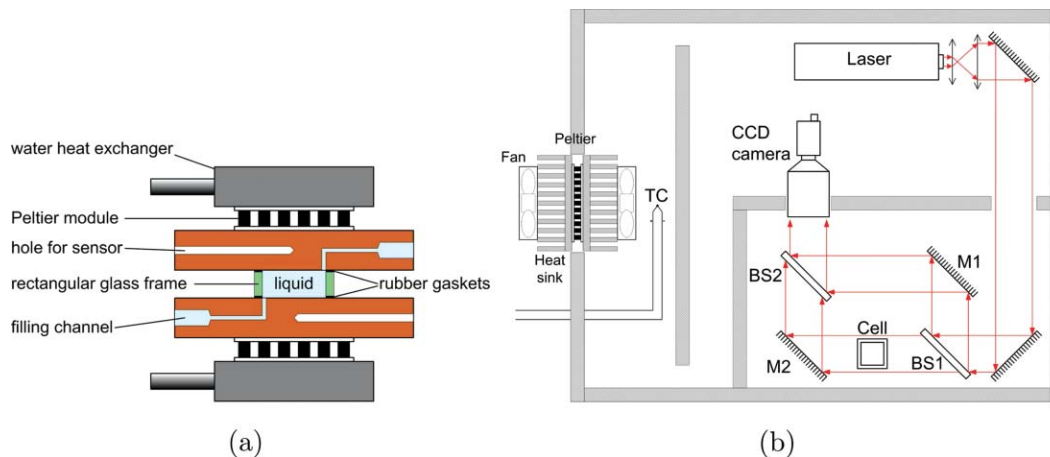[b)]Electronic mail: vshev@ulb.ac.be.

FIG. 1. (a) Cross section of the cell. (b) Scheme of the setup.

scattering[23–26] where a grating created by the interference of two laser beams is converted into temperature grating by a chemically inert dye. A periodic temperature field induces periodic field of concentration due to the Soret effect. Note that the relaxation time is short but a very large number of experimental runs in the same configuration are required for obtaining reliable results.[16]

In the method of optical digital interferometry (ODI; Ref. 27), the thermal and compositional variations are registered by observing the corresponding refractive index change of a diffusive media when a laser beam passes through the whole sample. In the case of a negative Soret coefficient ($S_T < 0$), the ODI method enables observation and evaluation of convective instability with time in the system. The sign change of S_T can be determined with some uncertainty by comparative analysis of the concentration fields (with and without convection) while approaching the point $S_T = 0$ from both sides. A variation of this technique with phase-shifting interferometer was used for measurement of diffusion coefficients in aqueous solutions.[28]

Optical interferometry is recognized as one of the most precise methods of measuring diffusion coefficients in liquids. An innovative point of this technique is the observation of the temperature and concentration fields in the whole cross section and not in the distinctive points. Although early attempts to use it for measuring the Soret coefficients date back to as early as 1957 (e.g., see Ref. 29), this method is currently not widely used. In our view, the major obstacle to it lies not in fundamental limitations but in a lack of properly developed image processing techniques. Our first instrument for measuring the Soret coefficients in liquids based on the optical digital interferometry was presented in Refs. 27 and 30. Since then we have considerably improved the cell design as well as data analysis.

The purpose of the current paper is twofold. First, to report recent improvements of the technique. Second, to report results of measurements of the Soret coefficients for the benchmark mixtures: 1,2,3,4-tetrahydronaphtalene (THN)–$C_{12}H_{26}$, THN–isobutylbenzene (IBB), and IBB–$C_{12}H_{26}$. The measured data by optical interferometry has been missing from the benchmark databases.

II. EXPERIMENTAL

A. Setup

For the measurements of Soret effect by means of optical diagnostics, we have adopted classical thermodiffusion cell with transparent lateral walls clamped between two thermostabilized copper blocks of $60 \times 50 \times 10$ mm^3 size. A close-up view of the cell is shown in Fig. 1(a). Laterally, liquid volume is enclosed in a rectangular cell, which is made of optical quality fused silica (custom made by Hellma) with external dimensions of $22 \times 22 \times 6.3$ mm^3, where $H = 6.3$ mm is the cell height; the wall thickness of 2.0 mm leaves $L = 18.0$ mm for the optical path in the fluid in both horizontal directions. The glass frame is sealed between the copper blocks with two gaskets of thermal conductive rubber of 0.2 mm thick (Chomerics, Cho-Therm 1674, thermal conductivity $\alpha = 1.0$ Wm^{-1}K^{-1}). The choice of the cell geometry and sealing material will be discussed in more details in Sec. III. To prevent excess stress in glass part caused by nonuniform clamping, four equal height spacers were additionally placed between the copper blocks and the glass frame.

Each copper block has a hole for a sensor (a calibrated NTC thermistor Epcos, B57861S861) and a channel for cell filling of 1.0 mm diameter. The external part of the channel accommodates standard connector for fluid management. The inlets of the channels into the cell are located at the opposite corners. The outgassed liquid is injected through the channel in the bottom plate. To outgas the liquid, a flow-through degasser (Systec, OEM Mini Vacuum Degasser 0001-6274) was interposed between the injecting syringe and cell. The degasser designed for outgassing solvents for high performance liquid chromatography (HPLC) applications does not affect the composition of liquid mixtures. Because the deep degassing requires a low flow rate, injection of liquid is done by a syringe pump (KD Scientific, model 210) with flow rate of 0.1 ml/min.

Each copper block is thermostabilized by Peltier element (Altec, 127-1.0 × 1.0-1.15, $P_{max} = 34$ W, $I_{max} = 3.9$ A). The temperature of Peltier elements back sides is kept constant by water heat exchangers connected to the circulating water bath (Haake F3). The thermal contact of Peltier elements with the

copper blocks on the working side and with the water blocks on the back sides was improved by inserting thin sheets of thermal conductive filler. The whole structure was gently fixed by a set of screws with equally applied torque.

The temperature of each copper block is regulated independently by two computer-driven PID controllers (Supercool, PR-59), enabling temperature stability of $\pm(0.01-0.02)$ K. Temperature logging is also provided by the controller with the resolution of 10^{-3} K. The data are recorded by computer with the desired sampling rate (up to 20 Hz).

To observe the concentration variation inside liquid mixtures, an optical digital interferometry was chosen. From a variety of different interferometer schemes (Rayleigh, Gouy, Fizeau, Michelson, and Mach–Zehnder), we have selected the last one because it allows simultaneous observation of the fringe pattern and the object itself and can easily treat the beam deflection problem.

Schematic drawing of the setup is shown in Fig. 1(b). The light source is a He–Ne laser (Thorlabs, HRR020) with a power of 2 mW and wavelength $\lambda = 632.8$ nm. The laser beam was expanded to cover the full area of the cell and then collimated. The collimated beam is splitted by 50R/50T plate beam splitter (50×50 mm^2 in size, Edmund Optics, NT45-854) into the reference and objective arms with cell assembly placed within the last one. Then both beams are redirected by 50 mm diameter mirrors of $\lambda/10$ flatness (Thorlabs, PF20-03-G01) at the second beam splitter to interfere. The resulting interferogram is recorded by CCD camera (JAI, CV-M4+CL) with 1392×1040 effective pixels on a 2/3 in. sensor and frame rate up to 24 fps. The camera is equipped with objective lens of 70 mm focal length and F2.2-32 aperture (Schneider, TXR 2.2/70-0902). The field of view covered by the imagine system is around 25 mm, so the resolution is 50 pixels/mm.

All the optical components are mounted on an optical bench plate of 600×450 mm^2, which is placed on top of the optical table but mechanically decoupled and thermally isolated from the latter. To improve the mechanical stability of the interferometer, all the elements were mounted on low rigid 25 mm diameter posts. To ensure the thermal stability of the interferometer during the experiment (up to 2–3 days), the whole setup including bearing bench plate is placed inside a box made of 3 cm thick foam thermal insulation material [shaded part in Fig. 1(b)]. The box is equipped with air-to-air cooling/heating assembly based on a Peltier element (Supercool, AA060-24220000, $P = 58$ W, $I = 3.1$ A) and driven by the dedicated PID controller of the same type as for the cell thermoregulation. A set of shields made of the same insulation material is inserted in the box to prevent air perturbation over optical paths. The temperature inside the box was kept equal to the mean temperature of liquid with residual fluctuations of ± 0.1 K.

B. Digital interferometry

Interferometry is a trusted and widely used optical technique for measurements of the refractivity of objects, from which related quantities like temperature or concentration can be determined.[31] For a given wavelength λ, the variation of the refractive index $n(x, z)$ includes temperature and concentration contributions,

$$\Delta n(x, z) = \left(\frac{\partial n}{\partial T}\right)_{T_0, C_0, \lambda} \Delta T(x, z) + \left(\frac{\partial n}{\partial C}\right)_{T_0, C_0, \lambda} \Delta C(x, z),$$
(1)

where $\Delta T(x, z)$ and $\Delta C(x, z)$ are the temperature and concentration changes at the point (x, z), here z-axis is the vertical direction. At the same time, Δn may be obtained from the phase difference $\Delta \varphi$, which is measured by interferometry:

$$\Delta n(x, z) = n(x, z) - n(x_0, z_0) = \frac{\lambda}{2\pi L} \Delta \varphi(x, z).$$
(2)

Here L is the optical path in liquid. As it follows from Eq. (2), the variation of refractive index Δn is equivalent to the change of the optical phase $\Delta \varphi$. Hereafter we will work with $\Delta \varphi$ as it is a measured value and is an additive quantity contrary to Δn.

In order to increase the accuracy of the phase evaluation of interference fringe patterns beyond the early fringe scanning technique, several procedures have been developed, such as the Fourier transform technique[32] or the temporal phase stepping technique.[33] These procedures are well established now.

1. Fringe analysis for phase-measuring interferometry

In optical interferometry, the change in phase between two coherent light waves (reference and objective ones) is used for visualization. The results of the optical interference of two light waves, an interferogram or fringe pattern, is taken by a sensor as a digital picture. We will shortly address the strategy of extracting phase information from the fringe pattern following Refs. 34 and 35 since this is fundamental for the discussed experimental technique. The intensity of two superposed waves of the same frequency is

$$i = |A_r + A_o|^2$$

where $A_r = a_r \cdot \exp(-i\varphi_r(x, z))$ and $A_o = a_o \cdot \exp(-i\varphi_o(x, z))$ are the amplitudes of reference and objective beams and φ_r, φ_o are the corresponding phase angles. Accordingly, the intensity in the fringe pattern at arbitrary time instant is

$$i(x, z) = i_0(x, z) + m(x, z) \cdot \cos[\Delta\varphi(x, z)],$$
(3)

where $\Delta\varphi(x, z) = \varphi_o(x, z) - \varphi_r(x, z)$ is the phase shift, $i_0(x, z)$ is the background intensity distribution, and $m(x, z) = 2|a_r| \cdot |a_o|$ is the modulation function.

A typical interference pattern recorded by a camera is presented in Fig. 2(a). A typical intensity profile over the horizontal line $z = H/2$ is shown in Fig. 2(b). It is possible to modify the spatial frequency of the fringes, $f_0 = \{f_{x0}, f_{z0}\}$, by changing the incident angle of the object and reference beams through adjusting the inclination angle of one of the mirrors.

Suppose that we have a spatial frequency in x-direction only ($f_0 = \{f_{x0}, 0\}$) then Eq. (3) can be rewritten as

$$i(x, z) = i_0(x, z) + c(x, z) \cdot \exp(2\pi f_{x0})$$
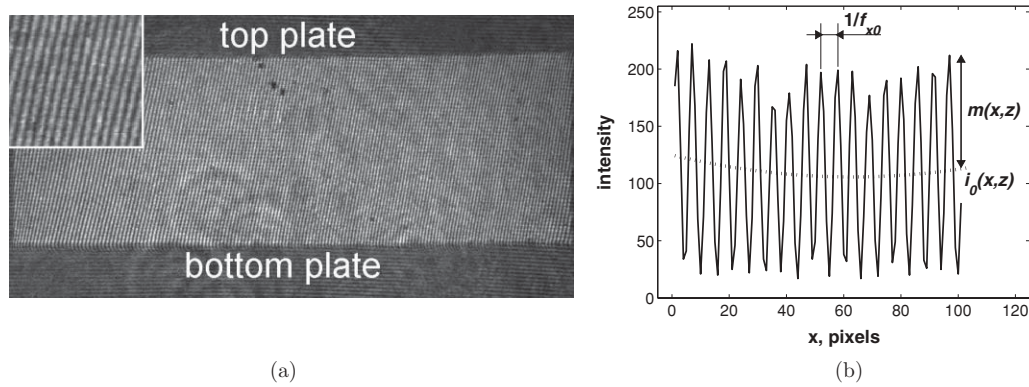$$+ c^*(x, z) \cdot \exp(-2\pi f_{x0}),$$
(4)

FIG. 2. (a) Typical interference pattern of 512×1024 pixels size covering full cell width with insert of magnified fringe pattern in top left corner. (b) Intensity profile on a horizontal line crossing an interferogram.

where $c(x, z) = 0.5 \cdot m(x, z) \cdot \exp[i \Delta\varphi(x, z)]$ is a complex amplitude. The superscript asterisk $(*)$ denotes a complex conjugate.

To calculate the phase shift $\Delta\varphi$, we have adopted a powerful two-dimensional (2D) Fourier transform technique. Originally developed for treating one-dimensional (1D) phase distributions,[32] this method was later adapted for 2D phase maps.[36] Performing the discrete Fourier transform of the array $i(x, z)$ yields

$$I(f_x, f_z) = I_0(f_x, f_z) + C(f_x - f_{x0}, f_z) \\ + C^*(f_x + f_{x0}, f_z). \quad (5)$$

The location of the terms I_0, C, and C^* in the Fourier domain and its intensity are shown in Figs. 3(a) and 3(b). If the introduced mirror tilt (correspondingly f_{x0} and f_{z0}) is appropriate, then these contributions are well separated in the Fourier domain. Both terms $C(f_x - f_{x0}, f_z)$ and $C^*(f_x + f_{x0}, f_z)$ contain equal information about the phase shift and a filter is applied in the Fourier space to keep only one of them. Filtering sets to zero all the frequencies except those belonging, for example, to the term, $C(f_x - f_{x0}, f_z)$. The resulting image is shown in Figs. 3(c) and 3(d), while the dashed curve shows the intensity distribution of the applied mask. During this procedure all the filtered out terms must be suppressed, but at the same time useful information within the remaining term $C(f_x - f_{x0}, f_z)$ should be preserved.

The 2D Fourier transform output is now rearranged by moving the spectrum on f_{x0} toward the origin of Fourier domain. It eliminates the carrier frequency f_{x0} and mathematically gives the term $C(f_x, f_z)$, see Figs. 3(e) and 3(f).

In performing the inverse Fourier transform, one can reconstruct both the amplitude and the spatial distribution of phase shift between object and reference beams. Accordingly

$$C(f_x, f_z) \rightarrow c(x, z) \text{ and } \Delta\varphi(x, z) = \arctan\left\{\frac{\mathrm{Im}[c(x, z)]}{\mathrm{Re}[c(x, z)]}\right\}. \quad (6)$$

A similar procedure is applied to the reference image for the evaluation of the phase shift $\Delta\varphi_{\mathrm{ref}}(x, z, t_{\mathrm{ref}})$, corresponding to reference time instant t_{ref}. The reference interferogram also determines the vector f_0. Subsequently, the phase shift $\Delta\varphi_{\mathrm{ref}}(x, z, t_{\mathrm{ref}})$ must be subtracted from $\Delta\varphi$ that corresponds

to the fringe pattern recorded after the change of an object. Correspondingly, the required phase distribution in Eq. (2) is the difference $\Delta\varphi - \Delta\varphi_{\mathrm{ref}}$. In this way, the method applies the holography principle and tracks the only posterior optical phase variation in the set of images following the reference image.

The phase difference calculated by arctangent function is wrapped, which means that it belongs to the range $(-\pi, \pi)$, see Figs. 4(a) and 4(b). It should be unwrapped to construct the continuous natural phase. It is a simple task for a one-dimensional case, while for a two-dimensional case and noisy fringes, sophisticated unwrapping techniques are required. As in our case phase maps typically have good quality, we adopt the following approach for phase unwrapping. The procedure starts at a pixel with well defined neighborhood assuming an error-free phase there. Following a spiral path the phase unwrapping is performed by comparing the wrapped phase with the previously validated neighbors. If the difference is less than π, the phase remains unchanged. If the difference between two pixels is more than π, the phase equals its wrapped phase minus 2π. If the difference is less than $-\pi$, the phase equals its wrapped phase plus 2π. By the end, the relative phase change between two pixels is placed in the range $-\pi$ and π and a smooth 2D phase map is obtained [see Figs. 4(c) and 4(d)].

It should be noted that the processing based on Fourier transform introduces two ambiguities to the extracted phase value. The sign ambiguity is caused by the fact that the term for filtering in the Fourier domain, $C(f_x - f_{x0}, f_z)$ or $C^*(f_x + f_{x0}, f_z)$, is usually chosen arbitrarily. The absolute value ambiguity is naturally arising from a wrapped character of the calculated phase. These ambiguities can be eliminated by using *a priori* information about the system (e.g., the known temperature of copper blocks and the mean concentration of liquid).

2. Subtraction of reference image

The two-dimensional phase distribution (map) contains information about many things. The wave-front is distorted by: all optical elements along the beam path $\Delta\varphi_{\mathrm{optics}}$, nonuniform air temperature $\Delta\varphi_{\mathrm{air}}$, temperature distribution
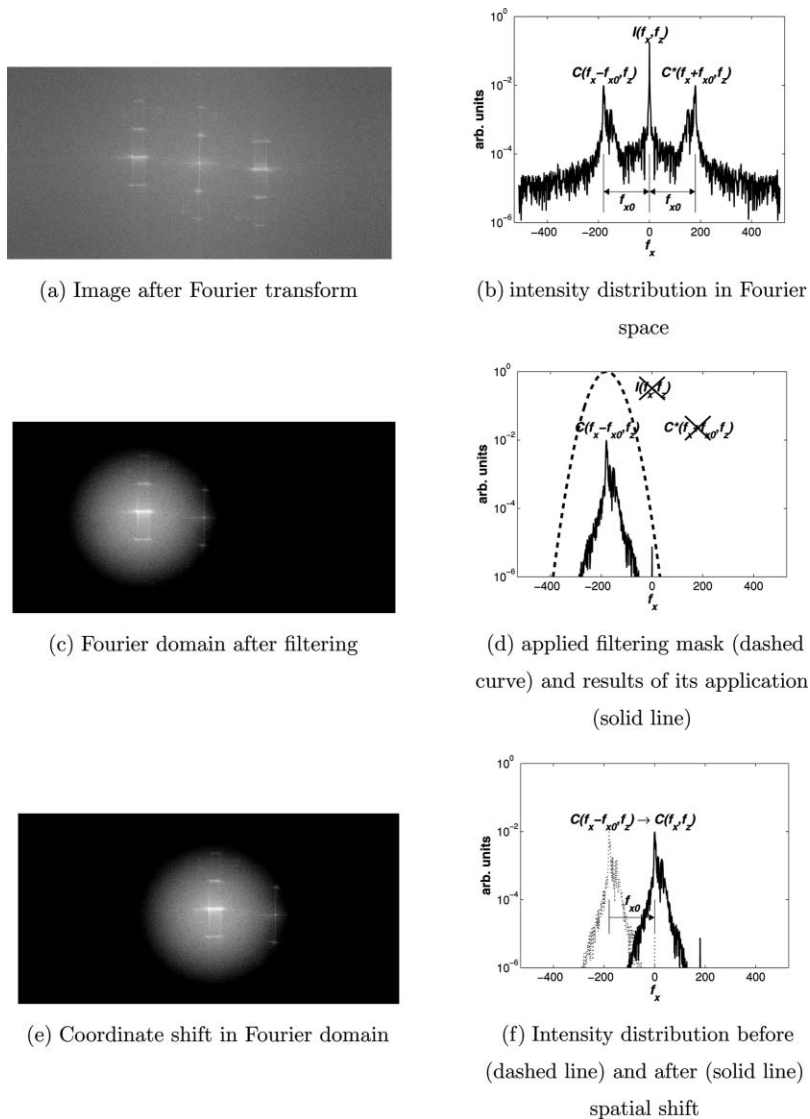
(a) Image after Fourier transform

(b) intensity distribution in Fourier space

(c) Fourier domain after filtering

(d) applied filtering mask (dashed curve) and results of its application (solid line)

(e) Coordinate shift in Fourier domain

(f) Intensity distribution before (dashed line) and after (solid line) spatial shift

FIG. 3. Steps of interferogram digital evaluation by 2D Fourier transform.
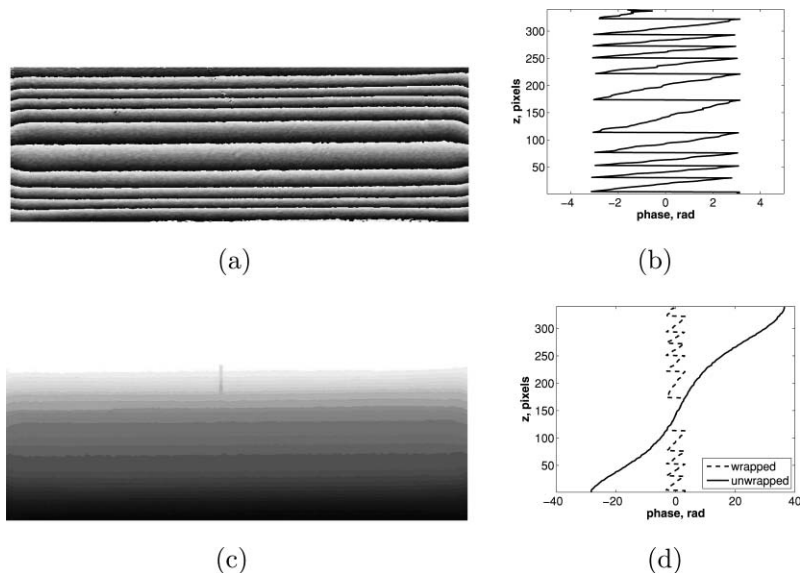

(a)

(b)

(c)

(d)

FIG. 4. Phase map resulting from Fourier processing. (a) Wrapped 2D distribution and (b) wrapped vertical profile; (c) unwrapped 2D map and (d) corresponding vertical profile.
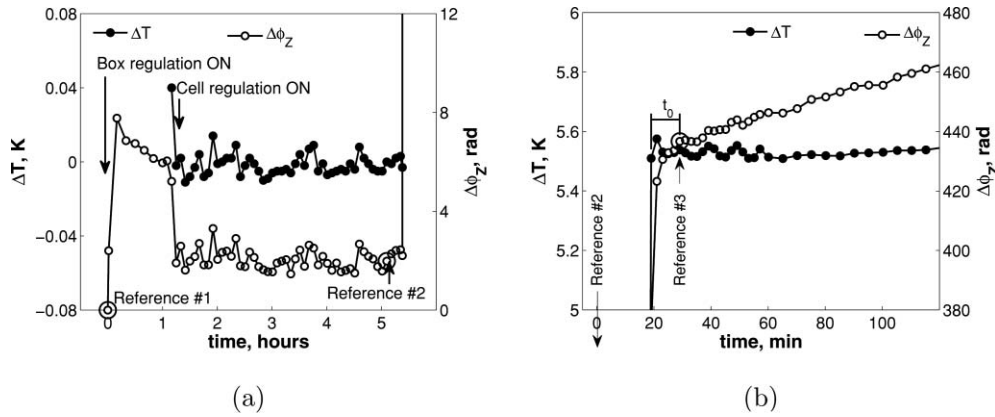
FIG. 5. Readings of temperature on sensors (left vertical axis) and phase variation measured optically (right vertical axis) with time. (a) Thermalization process at $T_0 = 25\,^\circ$C; (b) nonisothermal step.

in glass walls $\Delta\varphi_{\mathrm{glass}}$, temperature distribution in liquid bulk $\Delta\varphi_{\mathrm{th}}$, and finally by concentration distribution in the liquid $\Delta\varphi_C$:

$$\Delta\varphi = \Delta\varphi_{\mathrm{optics}} + \Delta\varphi_{\mathrm{air}} + \Delta\varphi_{\mathrm{glass}} + \Delta\varphi_{\mathrm{th}} + \Delta\varphi_C. \qquad (7)$$

Each particular interference pattern is formed either by all above factors or by some of them, depending on the state of instrument. An important part of overall processing routine is the separation of contributions. The advantage, which gives vast flexibility to this technique, is that any fringe pattern stored in the computer memory can be taken as a reference depending on the aim of the current processing step.

Let us briefly review this approach by considering an example of typical data processing steps. The first step traces the phase distribution during the instrument thermalization process. The step lasts 4–6 h and aims at stabilizing the temperature of the cell and interferometer at a mean temperature of $T_0 = 25\,^\circ$C. The very first image, Reference #1 in Fig. 5(a), is taken as a reference and processing continues during the entire isothermal step. In this case, the reference image keeps information about the initial state of the optics only ($\Delta\varphi_{\mathrm{ref}_1} = \Delta\varphi_{\mathrm{optics}}$) and the following phase variation is caused by possible optical path perturbations due to different mean temperatures of the air and the cell. In Fig. 5(a), the closed circles (see the left vertical axis) show alteration of temperature on sensors while the open circles (see the right vertical axes) show the corresponding variation of the phase $\Delta\varphi_z$. The importance of this step is to make sure of complete interferometer stability before the experiment is started. At the end of this step, a new reference image ($\Delta\varphi_{\mathrm{ref}_2} = \Delta\varphi_{\mathrm{optics}} + \Delta\varphi_{\mathrm{air}}$) must be chosen to process images after applying the thermal gradient over the cell [see Fig. 5(b)].

At the second step with typical duration of a few minutes, the phase variation is caused by the temperature differences in the glass wall and liquid bulk; the concentration contribution is negligibly small. Because the diffusion characteristic time, τ_D, is much larger than the thermal one, τ_{th}, Eq. (1) can be decomposed. For benchmark liquids, $\tau_D = H^2/D \approx 12$h while $\tau_{\mathrm{th}} = H^2/\chi \approx 200$ s, here χ is the thermal diffusivity of liquid. Thus the total phase variation at the observed point,

affected by temperature gradient, can be written as

$$\Delta\varphi = \Delta\varphi_{\mathrm{ref}_2}(x,z) + \Delta\varphi_{\mathrm{glass}}(z) + \Delta\varphi_{\mathrm{th}}(x,z). \qquad (8)$$

Assuming that the temperature distribution in the glass is linear ($T = T_0 + \Delta T[z/H - 0.5]$), glass thickness and temperature contrast factor for glass are well known, one can determine the contribution of glass walls $\Delta\varphi_{\mathrm{glass}}(z)$. Here H is the cell height,

$$\Delta\varphi_{\mathrm{glass}}(z) = \left[T_0 + \Delta T \left(\frac{z}{H} - 0.5 \right) \right]$$
$$\times \left(\frac{\partial n}{\partial T} \right)_{\mathrm{glass}} \frac{2\pi L_{\mathrm{glass}}}{\lambda},$$

where $L_{\mathrm{glass}} = 4$ mm is the optical path in glass. Substituting Eqs. (2) and (8) into Eq. (1), the optically measured temperature distribution inside liquid is

$$T(x,z,t)$$
$$= T_0 + [\Delta\varphi(x,z,t) - \Delta\varphi_{\mathrm{ref}_2}(z) - \Delta\varphi_{\mathrm{glass}}(z)]$$
$$\times \frac{\lambda}{2\pi L} \left(\frac{\partial n}{\partial T} \right)_{C_0, T_0}^{-1}. \qquad (9)$$

This optical measurements of the temperature field should be done as soon as the temperature field is established, i.e., within a few thermal times, $t \approx 3$–9 min. Later on optical measurements will start deviating from sensors readings due to concentration contribution, see Fig. 5(b) beyond point Reference #3. This deviation point, which appears after the temperature difference is established, is the reference point for the third image processing step—thermodiffusion separation, $\Delta\varphi_{\mathrm{ref}_3} = \Delta\varphi_{\mathrm{ref}_2} + \Delta\varphi_{\mathrm{glass}} + \Delta\varphi_{\mathrm{th}}$. This new reference interferogram holds information about all inputs into the optical phase except the concentration variation. Processing the next images with respect to this one provides the phase change, from which a full 2D map of concentration field is extracted

$$C(x,z,t) = C_0 + [\Delta\varphi(x,z,t) - \Delta\varphi_{\mathrm{ref}_3}(x,z)]$$
$$\times \frac{\lambda}{2\pi L} \left(\frac{\partial n}{\partial C} \right)_{C_0, T_0}^{-1}. \qquad (10)$$

3. Experimental limitations and precision of the method

The suggested method is based on Fourier processing, and its accuracy strongly depends upon the number of periods in the analyzed signal (i.e., the number of fringes in the interferogram). It means that the carrier fringe system has to be sufficiently dense. Small fringe spacing will also provide a distant peak in the Fourier domain, which is favorable for accurate filtering. At the same time, fringes have to be distinguished in the image. Fringe spacing of 4–6 pixels seems to be optimal for the method.

The other experimental conditions that strongly influence phase accuracy are the stability of light intensity (a good quality laser is needed) and the stability of interferometer. The last point is especially important. Perturbations of interferometer by environmental disturbances was analyzed in detail in Ref. 27 for a similar problem and it was shown that they can affect the measurement. For this particular reason, we took extra precautions for stabilizing the interferometer as mentioned in Sec. II A.

We tested the interferometer stability in two cases. The first test is when only the box thermoregulation is switched on; the other one is when the box and cell are thermostabilized at the mean temperature. All the tests last for at least 24 h. The variations of phase differences with time between the opposite extremes of the field of view (the top and bottom of the cell, for example) were analyzed. The typical value of the phase variation for the first test of interferometer is $\pm(0.1-0.2)$ rad. This value agrees well with the common accuracy of interferometry ($2\pi/50$), which can be found in literature.[35] Phase stability in the second test is $\pm(0.5-1.5)$ rad. This deterioration of the phase stability is not related to the interferometer itself, but to the stability of the cell thermal regulation, which was also confirmed by sensors readings [e.g., see Fig. 5(a)].

The unique feature of this method is that it traces the *transient* path of the system in the *entire* cross section of the cell. In this way it fits not only for the measurements of Soret coefficients but also for studying diffusive transport mechanism.

4. Beam deflection problem

It is well known that light beam refracts when passing through a medium with refractive index gradient. Both, a constant temperature gradient applied over the cell and a gradually increasing concentration gradient definitely cause refractive index variation, which in turn causes deflection of the object beam. This principle is used for measurements of transport coefficients in the beam deflection technique; for detail description, one can refer to Refs. 13, 20, and 37. In our technique it may play negative role, as the reference beam, which bypasses the cell, does not suffer from beam deflection. It means that the object beam may interfere with various regions of the reference beam at different time instants. For an ideally collimated beam with a perfect plane wave-front this point is not important. However, as the wave-front can be slightly disturbed in reality (e.g., by imperfect optical elements), it is better to exclude the problem *ab origin*. There
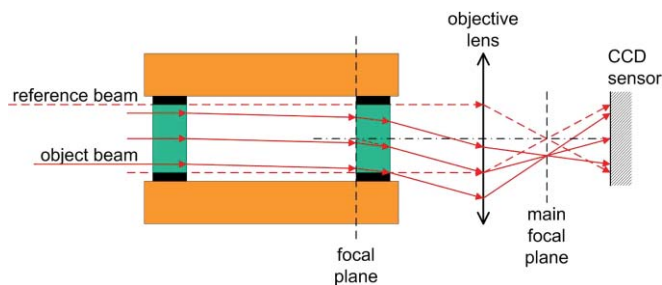

FIG. 6. Beam deflection problem.

is a natural way to make a correction for the beam deflection. Namely, an objective lens can return the beam refracted by an object into its initial position being properly focused (see Fig. 6). The problem is reduced to seeking the ideal working focal plane of the objective lens. To sum up, a simple practical rule can be applied for minimizing beam deflection effect on interferometry: imaging system has to be focused at the inner plane of the glass wall nearest to the camera, as it is drawn in Fig. 6. This agrees with conclusions of Ref. 38.

III. RESULTS AND DISCUSSION

A. Cell optimization

Another important aspect of the experiment design is the overall cell geometry. The cell geometry is a matter of serious optimization and we outline the most influential features. For example, the height of the cell should be large enough to allow easier manipulations with the probing beam. At the same time, it should not be too large since the time of the experiment is proportional to the cell height squared ($\tau_D = H^2/D$). The length of the cell should also be large enough since the signal measured by the instrument is directly proportional to the optical path (length). However, a long cell, which is advantageous for the beam deflection technique, is not the best choice for interferometry.

The cell geometry is important, but here we focus our attention on another factor that is really crucial for the measurement: the thermal design of the cell. Nonaccurate thermal design can completely discard all advantages of interferometry, since it determines the presence and intensity of the residual convection inside the cell. Due to drastically different characteristic times for transport of momentum and mass, the presence of convective flows in the diffusion cell will significantly alter the concentration field. For example, it was shown that the local convective vortex with a flow speed of 10–20 μm/s can completely homogenize concentration distribution in the region where this vortex exists.[27] So, the residual convection has to be reduced as much as possible.

When the thermal gradient is directed against gravity, the mechanical equilibrium in the cell is generally stable. But convection can easily appear at the lateral walls of the cell and in the corners where thermal perturbations are inevitable. In our first cell design,[27,30] we faced this problem of a horizontal temperature gradient at the corners. Using the advantage
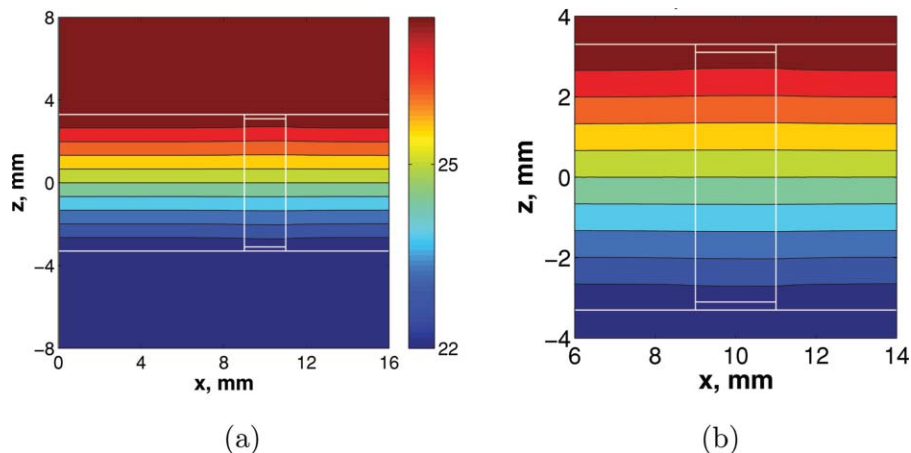
FIG. 7. (a) Computed temperature field in the half of the cell; white lines show the contact lines liquid/copper and liquid/glass, see entire geometry in Fig. 6. (b) The temperature distribution is in the magnified region near the contact line liquid/glass.

of the optical interferometry to monitor all the motions in the entire cross section of the cell during the transient process, the zones affected by convection were determined and excluded from consideration.

Unlike to the previous work, in the current study we have started with stationary heat transfer calculation of the supposed cell geometry with realistic boundary conditions. We used Comsol Femlab package as it allows easy generation and treatment of complex geometries. The thermal properties of copper, quartz glass, water, rubber, and air are taken from a physics handbook. Working on the design of a new cell we have considered different feasible cell geometries, and drew a conclusion that almost complete elimination of lateral temperature gradients is possible, but in very few cases. One of them finally chosen by us is the following: *flat* copper plates (without protrusions and grooves) cover not only the liquid but also the glass walls. Sealing between glass and copper is made of material with thermal conductivity close to that of glass. Nowadays such materials are commercially available as thermal conductive composite rubber. One can see the sketch of the geometry in Figs. 1(a) and 6. The results of numerical simulation, shown in Figs. 7(a) and 7(b), demonstrate the absence of horizontal temperature gradients near the walls. The experimental observations of the temperature field made by the interferometer confirm the absence of lateral heat fluxes as well [see Fig. 8(a)]. The concentration field resulting from thermodiffusion separation in this cell, [Fig. 8(b)] also demonstrates the absence of convective motion since the concentration distribution is practically nondisturbed and varies only along the temperature gradient.

B. Extraction of transport coefficients

1. Fitting equation for full path

The present technique gives a unique possibility of increasing measurement accuracy by providing information about concentration distribution along the whole thermodiffusion path. In fact, the method gives a two-dimensional concentration field, although the distribution itself is almost one-dimensional. This extensive information can be used for evaluation of convection, but in the case when convection is really negligible, the 1D approach can be used for mathematical description of measurements. Each time a measurement is taken, a full concentration distribution over the thermodiffusion path is determined. The solution of thermodiffusion equations for convection-free case can be written as follows:[27]

$$C(z,t) = C_0 + C_0(1 - C_0) S_T \Delta T$$

$$\times \left[\frac{1}{2} - \frac{z}{H} - \frac{4}{\pi^2} \sum_{n,\text{odd}}^{\infty} \frac{1}{n^2} \cos\left(\frac{n\pi z}{H}\right) \right.$$

$$\left. \times \exp\left(-n^2 \frac{t}{\tau_r}\right) \right]. \tag{11}$$

Here $\tau_r = H^2/\pi^2 D$ is the relaxation time, D and S_T are the diffusion and the Soret coefficients, H is the height of the cell. The sign between the two first terms in Eq. (11) depends on the choice of the component which we follow: lighter or heavier. The sign is negative $(-)$ in the case of heavier component
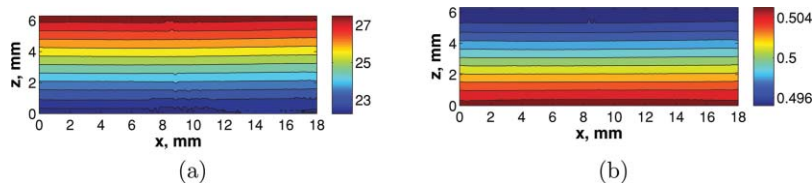

FIG. 8. Stationary fields in THN–$C_{12}H_{26}$ measured by interferometer. (a) Temperature field; (b) concentration field.
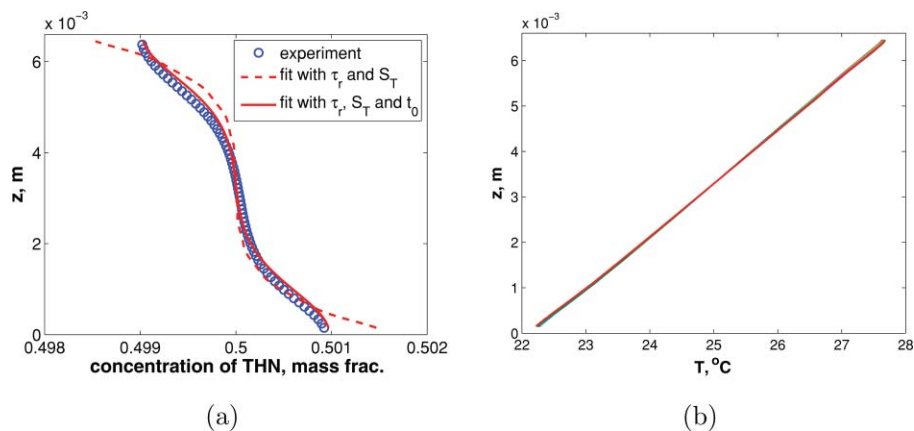
FIG. 9. (a) Fitting optimization; experimentally measured $C(z)$ (open circles) and its fitting curves with two (dashed curve) and three (solid curve) fitting parameters for THN–$C_{12}H_{26}$ at $t = 0.16\,\tau_r$, (b) ten snapshots of temperature profile for THN–$C_{12}H_{26}$ display small oscillations $T(z)$ near horizontal walls due to temperature instability of copper plates.

(as it is written) and positive $(+)$ in the case of a lighter component.

In Eq. (11) there are two unknown parameters, S_T and τ_r. The simplest procedure to find them is to compare the concentration measured at point z_i at time t_j with its value from Eq. (11) using the initial guess for S_T and τ_r. Then fitting is done iteratively by using the Nelder–Mead algorithm (MATLAB), which minimizes the misfit function

$$\delta C(z,t) = \sum_{i,j}^{k,m} [C_{\text{exper}}(z_i, t_j) - C_{\text{theor}}(z_i, t_j)]^2, \qquad (12)$$

by varying the fitting parameters S_T and τ_r. The number of spatial pixel points in the experimental dataset is around $k = 340$ and the number of acquired images is varied in limits $200 < m < 800$. So, the fitting is done with the matrix of at least $k \times m = 340 \times 200$ size. Thanks to such big amount of data, this approach gives satisfactory results. However there exists a less obvious fitting parameter which allows essential improvement of the fitting results. This fitting variable, t_0, can be called *initial time*.

The point is that the reference image for extracting concentration distribution is not necessarily located at the very beginning of the separation step [see Fig. 5(b)]. Note that this image has to be taken only after the temperature profile is completely established, see Sec. II B 2. A reliable reference image can often be found 3–9 min after the visible separation starts, although in the above fitting the time of the reference image is $t = 0$ and $C_{\text{exper}}(z, 0) = C_0$, which is not precise. This can be resolved by introducing third fitting variable t_0. Then the theoretical anticipation for the experimental concentration profile is given by

$$C_{\text{theor}}(z,t) = C(z, t_0 + t) - C(z, t_0) + C_0, \qquad (13)$$

where both terms $C(z, t_0 + t)$ and $C(z, t_0)$ are calculated according to Eq. (11). Such correction provides a much better fit to the experimental data as it is shown in Fig. 9(a). Note that the snapshot of the data is presented at the time $t = 0.16\,\tau_r$, which is far from a steady state. The open circles present experimental results; the dashed curve shows $C_{\text{theor}}(z, t)$ when two fitting parameters were used; the solid

line shows $C_{\text{theor}}(z, t)$ when three fitting parameters were used. We should emphasize that the margins of the new fitting parameter t_0 are known from the experiment [see Fig. 5(b)] with rather good accuracy.

Finally, we will discuss the source of errors, which is less evident and more difficult to treat. It arises from the fact that the temperature of the copper plates is not strictly constant; it has some minor fluctuations as the regulation is active. In this case, the experimentally observed profile, considered as a pure concentration one, has some input of the thermal nature. This input appears due to the optical coupling of both values (i.e., $\Delta\varphi_{\text{th}} = \text{const}[1 + \delta(t)]$) and can be either negligibly small $(\max|\delta(t)| \to 0)$ or noticeable depending on the ratio of the respective contrast factors and the temperature fluctuation value. This effect can be seen in Fig. 9(b) where ten snapshots of the temperature profile are shown for THN–$C_{12}H_{26}$. Temperature fluctuations can be seen by eye near the horizontal walls where their amplitude achieves 0.5% of a signal at the worse case.

Our dedicated study showed that the amplitude of temperature disturbances rapidly decays and does not penetrate deeply into the liquid bulk. However, in some cases [as shown in Fig. 9(b)] when other uncertainties are added to the signal (e.g., due to the low contrast factor) we have to consider near-wall regions as corrupted and crop out them from consideration. For different reason similar approach was applied in Ref. 27. Comparison of S_T obtained on the basis of such a transient approach and from a steady state justifies the procedure.

C. Benchmark mixtures

Chemicals used for experiments are dodecane, $C_{12}H_{26}$, (Acros Organics, 99%), IBB (Acros Organics, 99.5%), and THN (Acros Organics, 98+%). The above substances were used without further purification. Then three binary solutions were mixed according to the required weight fraction 50 wt. %. Temperature difference applied over the cell was constant in all the cases and equal to $\Delta T = 5.53 \pm 0.02$ K, while the mean temperature was $T_0 = 298$ K. The Soret

coefficients for all the three mixtures are positive. So, no hydrodynamic instabilities are expected for these mixtures.

The values of the refractive index variation with temperature and concentration, respectively, $(\partial n/\partial T)_{T_0,C_0}$ and $(\partial n/\partial C)_{T_0,C_0}$, (the so-called contrast factors), are required for the measurement of species separation. We rely on the values provided in Ref. 24, where the measurements were performed by a precise and reliable technique using the same quality chemicals provided by the same manufacturer.

Each experiment consists of two steps and at each of them the images are acquired at specified rate. First, a Soret separation step starts when the temperature gradient is established. This step lasts for about 10–12 h. Second, a relaxation step starts when the temperature gradient is removed with the purpose of the measurement of the diffusion coefficients in an isothermal regime. This step also takes about 10–12 h. To summarize, during one experiment each coefficient is measured twice: at the *Soret* step we measure diffusion D and Soret S_T coefficients in a transient regime. An

(a) $\Delta C(t)$ for THN-C$_{12}$H$_{26}$

(b) $C(z)$ for THN-C$_{12}$H$_{26}$

(c) $\Delta C(t)$ for THN-IBB

(d) $C(z)$ for THN-IBB

(e) $\Delta C(t)$ for IBB-C$_{12}$H$_{26}$
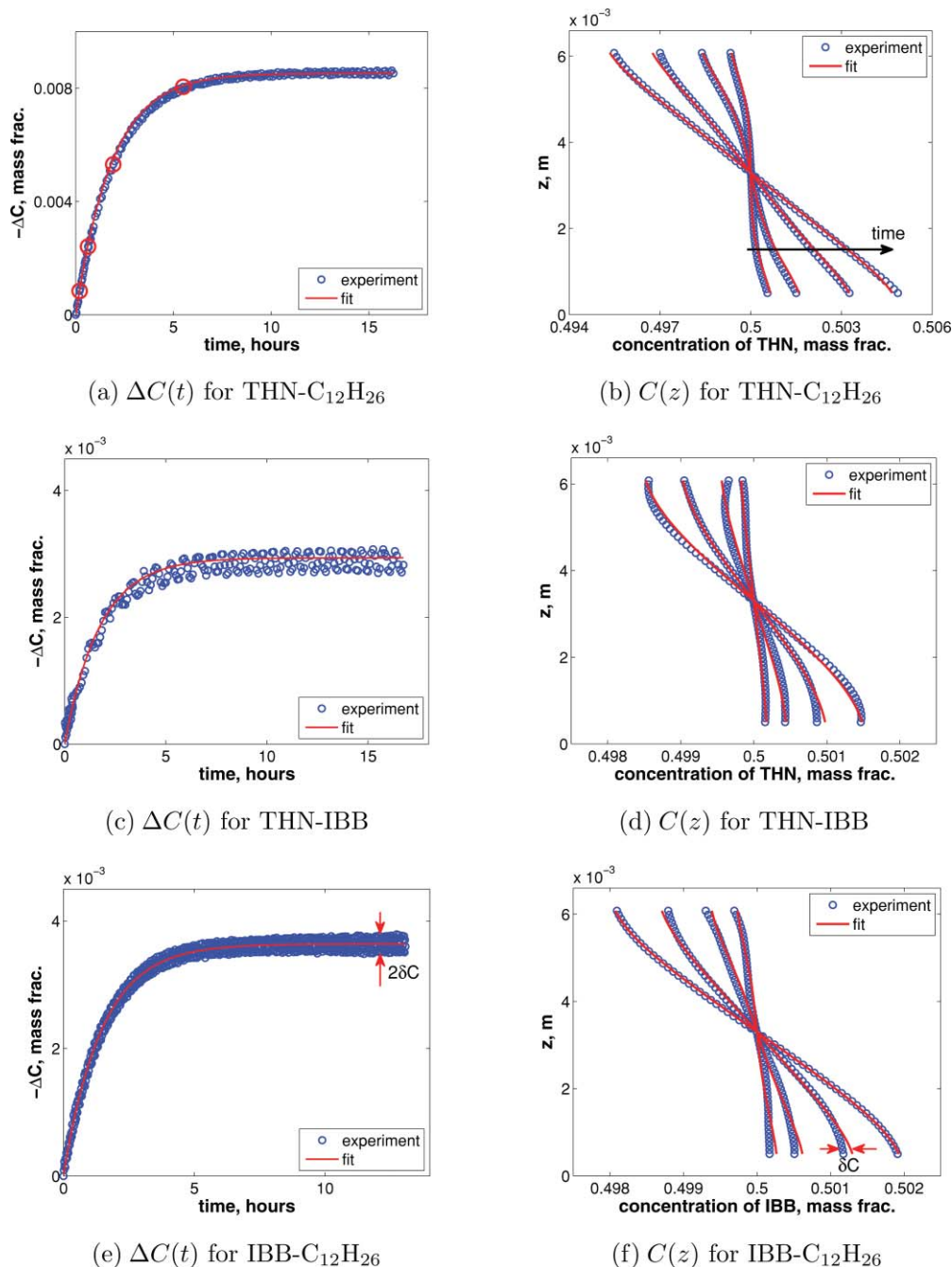
(f) $C(z)$ for IBB-C$_{12}$H$_{26}$

FIG. 10. Experimental results for benchmark liquids: open circles indicate experimental points and solid curves outline their fitting. Pictures on left side (a), (c), and (e) show separation of component with time. Pictures on the right side (b), (d), and (f) show the concentration profiles over the height of the cell at nonsteady regime with progress in time, $t/\tau_r = 0.11$, 0.33, 1.0, and 3.0. The curve for the smallest time is close to be vertical; τ_r is the relaxation time.

TABLE I. Evaluation of SNR. Comparison of refractive index variation due to concentration and thermal impacts for investigated mixtures.

Mixture	$\left(\frac{\partial n}{\partial T}\right)$[a] $\times 10^{-4}$ (1/K)	δn_T $\times 10^{-6}$	$\left(\frac{\partial n}{\partial C}\right)$[a] $\times 10^{-2}$(1/K)	ΔC $\times 10^{-3}$	Δn_C $\times 10^{-4}$	SNR
THN–C$_{12}$H$_{26}$	−4.41	8.82	11.7	8.54	9.99	113
IBB–C$_{12}$H$_{26}$	−4.54	9.08	6.28	3.64	2.29	25
THN–IBB	−4.76	9.52	5.44	2.88	1.57	16

[a]Data from Ref. 13.

alternative value of S_T is determined from the achieved steady state

$$S_T = -\frac{1}{C_0(1 - C_0)}\frac{\Delta C_{\mathrm{st}}}{\Delta T}, \tag{14}$$

and an alternative value of D is obtained from the *relaxation* step in an isothermal regime.

The majority of the methods used for measurements of transport coefficients work with point measurements at a given time or with a gradient. Optical digital interferometry enabled measurements of ΔC between arbitrary points and, correspondingly, reproduces the concentration field in the whole two-dimensional cross section.

The time-dependencies $\Delta C(t)$ for the three benchmark mixtures are shown in Fig. 10 on the left side while the spatial concentration distributions for the same liquid are shown on the right side. The concentration profiles are presented at four different times which are very far from the steady state: $t/\tau_r = 0.11, 0.33, 1.0,$ and 3.0. Note, that the stationary values ΔC_{st} in Figs. 10(a), 10(c), and 10(e) should be divided by $\Delta T < 5.53$ K in Eq. (14) as some small regions near the horizontal walls are cropped out; see the right sides of Fig. 10. The succession of the profiles $C(z)$ demonstrates the development of the diffusion process with time. The small fluctuations of the fitting curve near the horizontal walls, shown via δC in Fig.10(f), result into the scattering of the points on the separation curve $\Delta C(t)$ which is more than satisfactory. Nowadays the presented technique is the only one, which can display evolution of the concentration field with time, as shown on the right pictures in Fig. 10.

At the first glance, the separation curves $\Delta C(t)$ for various mixtures exhibit different scattering of data points. The reason for that becomes clear if we consider the optical properties of media. Let us calculate the variation of the refractive index of liquid due to temperature inconstancy,

$\delta n_T = \delta T(\partial n/\partial T)$ where $\delta T = \pm 0.02$ K, and the total refractive index difference due to species separation, $\Delta n_C = \Delta C(\partial n/\partial C)$. Then one can deduce a kind of signal-to-noise ratio (SNR), which is the ratio of the above values, $\Delta n_C/\delta n_T$. These data are summarized in Table I. The contrast factors $(\partial n/\partial C)_{T_0,C_0}$ for the last two mixtures are small and it results in poor SNR. Ratio signal/noise for THN–C$_{12}$H$_{26}$ is the largest because of the largest contrast factor and the largest separation ΔC.

Although the SNR value is somehow overestimated (because this specific noise corrupts a part of data only), it can provide a clear idea about method applicability range. For example, in the regions where the contrast factor $\partial n/\partial C$ vanishes, or separation decreases due to vanishing S_T, the SNR drops down with the accuracy of the technique. There is an evident way to increase the SNR by increasing temperature stability, but the capability of this way is limited. As soon as temperature stability will rise from, say ± 0.01 to ± 0.001 K (it will extend SNR by an order of magnitude), an optical noise will enter into play, which is much more difficult to suppress. To conclude, the transport coefficients can be measured with a good accuracy for the values of SNR as low as 10–15.

The measured values of diffusion and Soret coefficients for the three mixtures are given in Table II together with the original benchmark references. The thermodiffusion coefficient $D_T = D \cdot S_T$ can be easily calculated. The results were obtained using three-parameters fitting procedure (D, S_T, t_0) with the value of the parameter t_0 close to the measured one, see Fig. 5(b). Two values for diffusion coefficient are given in Table II: from isothermal and nonisothermal measurements. For comparison with the benchmark data an average value of D is used.

For all the mixtures, we have got an excellent agreement for both diffusion and Soret coefficients, our measurements differ from the previous benchmark values by 1%–3%.

TABLE II. Diffusion and Soret coefficients for three benchmark mixtures.

	Quantity	THN–C$_{12}$H$_{26}$	THN–IBB	IBB–C$_{12}$H$_{26}$
This work	$D^a{}_S$, 10^{-10} m^2/s	6.16 ± 0.05	8.6 ± 0.28	9.4 ± 0.22
	D^b, 10^{-10} m^2/s	6.37 ± 0.05	8.43 ± 0.28	9.23 ± 0.22
	D^c, 10^{-10} m^2/s	6.27 ± 0.29	8.52 ± 0.12	9.32 ± 0.12
	S_T, 10^{-3} 1/K	9.24 ± 0.01	3.29 ± 0.11	3.98 ± 0.08
Benchmark values, Ref. 14	D, 10^{-10} m^2/s	6.21 ± 0.06	8.5 ± 0.6	9.5 ± 0.4
	S_T, 10^{-3} 1/K	9.5 ± 0.3	3.3 ± 0.3	3.9 ± 0.1

[a]Diffusion coefficient measured during Soret separation.
[b]Diffusion coefficient measured at isothermal conditions.
[c]Mean value of diffusion coefficient between isothermal and nonisothermal conditions.

IV. CONCLUSIONS

We have discussed in depth the use of ODI for the measurement of diffusion and Soret coefficients. Although the first impression may give an idea that the ODI technique is a combination of known elements (Soret cell and interferometer), the proper design of the novel instrument reveals the unique feature of this method—the observation of the temperature and concentration fields in a *transient* regime in the *whole* cross section, and not just in distinctive points. Nowadays the presented technique is the only one, which can display evolution of the concentration field with time, as shown on the right pictures in Fig. 10.

From the first time when we presented this technique,[27] the cell design as well as the image processing performance have been considerably improved. One of the targets of this paper was to describe this technique in such a way that it becomes practical and widely employable. With this goal in mind, the successive steps of the entire procedure of the ODI technique were presented with a focus on its capability to measure the diffusion and Soret coefficients. Among all the steps, four have been selected for in-depth consideration: the fringe analysis, the choice of reference images, the thermal design of the cell, and the multiparameter fitting procedure. In addition, the sources of possible uncertainties were identified and guidelines were drawn for an improvement of the accuracy of the results.

With the renewed ODI technique, we have measured the diffusion and the Soret coefficients for the three benchmark systems composed of $C_{12}H_{26}$, IBB, and THN at a mean temperature of 25°C and 50 wt. % in each component. The results showed an excellent overall agreement with the proposed benchmark references. The data measured by optical interferometry were missing from the benchmark databases. As a conclusion, our results are in the general trend of other ones, and prove that the suggested technique is competitive, while having some attractive advantages.

ACKNOWLEDGMENTS

[1] C. Soret, Arch. Sci. Phys. Nat. Geneva **2**, 48 (1879).
[2] K. Ghorayeb, A. Firoozabadi, and T. Anraku, SPE J. **8**(2), 114 (2003).
[3] F. Montel, Entropie **184–185**, 86 (1994).
[4] F. M. Richter, N. Dauphas, and F.-Z. Tenga, Chem. Geol. **258**, 92 (2009).
[5] K. Harstad and J. Bellan, Int. J. Multiphase Flow **26**, 1675 (2000).
[6] R. M. Schmitt, Annu. Rev. Fluid Mech. **26**, 255 (1994).
[7] F. J. Bonner and L.O. Sundelöf, Z. Naturforsch. C **39**, 656 (1984).
[8] A. Leahy-Dios, M. M. Bou-Ali, J. K. Platten, and A. J. Firoozabadi, J. Chem. Phys. **122**, 234502 (2005).
[9] P. Blanco, M. M. Bou-Ali, J. K. Platten, D. A. de Mezquia, J. A. Madariaga, and C. Santamaría, J. Chem. Phys. **132**, 114506 (2010).
[10] A. Königer, H. Wunderlich, and W. Köhler, J. Chem. Phys. **132**, 174506 (2010).
[11] S. A. Putnam and D. G. Cahill, Rev. Sci. Instrum. **75**, 2368 (2004).
[12] M. Hartung and W. Köhler, Rev. Sci. Instrum. **78**, 084901 (2007).
[13] A. Königer, B. Meier, and W. Köhler, Philos. Mag. **89**, 907 (2009).
[14] J. K. Platten, M. M. Bou-Ali, P. Costeseque, J. F. Dutrieux, W. Koehler, C. Leppla, S. Wiegand, and G. Wittko., Phil. Mag. **83**, 1965 (2003).
[15] T. Pollak and W. Köhler, J. Chem. Phys. **130**, 124905 (2009).
[16] J. K. Platten, ASME J. Appl. Mech. **73**, 5 (2006).
[17] J. K. Platten, M. M. Bou-Ali, and J. F. Dutrieux, Philos. Mag. **83**, 2001 (2003).
[18] P. Blanco, M. M. Bou-Ali, J. K. Platten, P. Urteaga, J. A. Madariaga, and C. Santamaría, J. Chem. Phys. **129**, 174504 (2008).
[19] P. Kolodner, H. Williams, and C. Moe, J. Chem. Phys. **88**, 6512 (1988).
[20] R. Piazza, Philos. Mag. **83**, 2067 (2003).
[21] M. Giglio and A. Vendramini, Appl. Phys. Lett. **25**, 555 (1974).
[22] H. Cabrera, L. Martin-Lopez, E. Sira, K. Rahn, and M. Garcia-Sucre, J. Chem. Phys. **131**, 031106 (2009).
[23] K. Thyagarajan and P. Lallemand, Opt. Commun. **26**, 54 (1978).
[24] G. Wittko and W. Köhler, Philos. Mag. **83**, 1973 (2003).
[25] C. Leppla and S. Wiegand, Philos. Mag. **83**, 1989 (2003).
[26] P. Polyakov and S. Wiegand, J. Chem. Phys. **128**, 034505 (2008).
[27] A. Mialdun and V. Shevtsova, Int. J. Heat Mass Transfer **51**, 3164 (2008).
[28] S. Maruyama and A. Komiya, J. Flow Visualization Image Process. **13**, 243 (2006).
[29] L. G. Longsworth, J. Phys. Chem. **61**, 1557 (1957).
[30] A. Mialdun and V. Shevtsova, Microgravity Sci. Technol. **21**, 31 (2009).
[31] W. Merzkirch, *Flow Visualization* (Academic, Orlando, 1987).
[32] M. Takeda, H. Ina, and K. Kobayashi, J. Opt. Soc. Am. **72**, 156 (1982).
[33] K. Creath, "Phase-measurement interferometry techniques," in *Progress in Optics*, edited by E. Wolf (North-Holland, Amsterdam, 1988), Vol. **XXVI**, p. 349.
[34] H. J. Tiziani, Opt. Quantum Electron. **21**, 253 (1989).
[35] M. Hipp, J. Woisetschläger, P. Reiterer, and T. Neger, Measurement **36**, 53 (2004).
[36] W. W. Macy, Jr., Appl. Opt. **22**, 3898 (1983).
[37] K. J. Zhang, M. E. Briggs, R. W. Gammon, and J. V. Sengers, J. Chem. Phys. **104**, 6881 (1996).
[38] C. Mattisson, D. Karlsson, S. G. Pettersson, G. Zacchi, and A. Axelsson, J. Phys. D: Appl. Phys. **34**, 3088 (2001).